PCCP

ROYAL SOCIETY OF CHEMISTRY

PAPER

View Article Online
View Journal | View Issue



Cite this: *Phys. Chem. Chem. Phys.*, 2025, **27**, 9478

# Hg(II) causes photoluminescence quenching of pyrene inside a blue emitting ionic liquid-derived crystalline nanoball†

Najmin Tohora,[a] Rajkumar Sahoo,[b] Sabbir Ahamed,[a] Jyoti Chourasia,[a] Shubham Lama,[a] Manas Mahato,[a] Shreya Ali[a] and Sudhir Kumar Das *[a]

This report presents the self-assembly of a blue-emitting ionic liquid (IL), NTIL, prepared by combining pyrene butyrate with a quaternary phosphonium ionic liquid (IL) through a straightforward ion exchange method. Water-dispersible crystalline nanoparticles, referred to as nNTIL, were developed using a reprecipitation technique. The nanocrystalline and molecular-level organization of pyrene moieties within these nanoparticles was validated using various spectroscopic, microscopic, and calorimetric analyses. Pyrene counterparts in the nanocrystalline nanomaterials demonstrate a strong tendency to self-associate when excited. The self-aggregation of pyrene moieties in their electronic excited state is found to be pronounced and beyond the simple excimeric dimerization process. $Hg^{2+}$ ions cause strong photoluminosity quenching, which is found to be pronounced owing to the strong π–π stacking interactions among the pyrene moieties inside the crystalline nanoball due to the strong electrostatic interaction between pyrene butyrate and $Hg^{2+}$ ions, causing further clotting of water dispersed nanoparticles. The induction of further coagulation of nNTIL by $Hg^{2+}$ ions was validated through scanning electron microscopy (SEM) and energy dispersive X-ray spectroscopy (EDS) analysis. Analysis of the quenching of photoluminosity through photoluminescence lifetime decay analysis revealed that the process is dynamic. The practical applications of nNTIL were illustrated through analyses of water and soil samples, paving the way for applications in diverse fields. Furthermore, we investigated the sensor's effectiveness in detecting $Hg^{2+}$ ions using affordable test strips. The present report introduces the fabrication and implications of metal-sensitive IL-based low-dimensional materials exhibiting remarkable photophysical properties compared with traditional ones.

Received 10th December 2024,
Accepted 8th April 2025

DOI: 10.1039/d4cp04660a

rsc.li/pccp



## 1. Introduction

Ionic liquids (ILs) are a distinctive class of organic salts that have melting points below 100 °C. Unlike conventional ionic salts, the propensity for crystal formation in ILs is substantially diminished because of sterically incompatible ions, which leads to a substantial reduction in their melting points.[1–3] They are recognized for their relatively low toxicity and biocompatibility, as well as their antibacterial properties and selective catalytic capabilities. They can be tailored to meet specific requirements by altering their constituent ions and incorporating various functional groups into their structures.[3] This versatility allows for a wide range of applications, such as extraction and separation processes, the formulation and delivery of active pharmaceutical ingredients (APIs), biocatalysis, sensor development, gel and molecular probe synthesis, electrochemistry, energy efficiency enhancements, and the design of microemulsions.[4,5] ILs are being increasingly utilized to replace conventional solvents and electrolytes, evolving into distinct functional media, fluids, and materials. This shift marks a new trend to explore photonic materials that have gained attention in recent years.[6–10] The integration of ILs with photonic materials has notably enhanced their applicability across a range of optoelectronic applications. In these contexts, ILs act as versatile building blocks, forming the basis for innovative photonic materials.[11] These new materials tend to offer significant advantages over traditional molecular counterparts. Because of the high modularity of ILs, specific functionalization tailored for particular optoelectronic applications can be achieved. This is often accomplished through ion-exchange metathesis reactions or by introducing specific functional groups into ILs' structure, resulting in the formation of novel

[a] *Department of Chemistry, University of North Bengal, Raja Rammohunpur, Darjeeling, West Bengal 734013, India. E-mail: sudhirkumardas@nbu.ac.in*
[b] *Department of Chemistry, Indian Institute of Technology, Kharagpur, West Bengal 721302, India*

† Electronic supplementary information (ESI) available See DOI: https://doi.org/10.1039/d4cp04660a

ion-containing materials. Such photonic materials maintain the essential properties of their original counterparts while incorporating the beneficial characteristics of ILs, leading to the development of advanced photo-functional materials. However, much of the existing literature focuses on the role of ILs as solvents and electrolytes, along with the advancement of high-performance functional materials.[12,13] Research exploring the application of ILs in the design and development of photonic materials for various optoelectronic functions, such as photon upconversion, white light generation, and FRET-mediated down conversion, remains relatively scarce. Furthermore, nanoparticles can be synthesized through straightforward methods by adjusting the length of the aliphatic side chains within the ILs. These nanoparticles hold promise for applications in sensing, biomedical fields, and energy conversion.[14–18]

In today's world, nanoparticles play an integral role in various aspects of life primarily because of their distinctive intrinsic properties, such as enhanced surface-to-volume reactivity relative to bulk materials, distinct atomic and electronic structures, and notable morphological characteristics.[19,20] Recently, nanomaterials have emerged as a focal point in biomedical research, finding applications in therapeutics, cellular imaging, drug delivery systems, and biological sensing.[21,22] Ionic liquids (ILs) have increasingly been recognized for their role in the synthesis of these biologically active nanoparticles, serving as effective templates or solvents.[23] Their ability to form cage-like hydrogen bonds enhances self-organization and molecular aggregation.[24] Nanomaterials derived from ILs present a range of promising applications across the biomedical landscape, as well as in sensing and energy conversion technologies.[25,26]

Pyrene and its derivatives are exceptional aromatic hydrocarbons known for their unique properties and broad range of applications. These include aggregation-induced fluorescence characteristics, significant delocalization of π electrons, excimer formation in the excited state, strong UV-visible absorption and emission characteristics, high quantum yield, and prolonged photoluminescence lifespan.[27–31] Additionally, the monomer and excimer exhibit distinct responses when interacting with various metal ions, dye molecules, and biomolecules.[27,32–34] These properties enable their use as core components in diverse photoelectronic devices, including excimer lamps, lasers, and photovoltaics.[35] Hence, modulating the photophysical properties of pyrene moieties inside the core of ILs would be more beneficial for fabricating IL-based photonic materials and for multifaceted optoelectronic applications.

The investigation of heavy and transition-metal ions for detection and quantification has gained attention because of their significant harmful effects on the environment and living organisms.[36] Among these metals, mercury stands out as the most toxic, associated with numerous serious health issues such as cardiovascular diseases, kidney toxicity, neurotoxic effects, cancer, immune system impairment, and adverse reproductive and developmental outcomes.[37–41] Mercury poses risks in all its oxidation states (0, +1, and +2[37]), despite variations in their solubility and potential for redox reactions. Its chemical forms primarily determine the ecological and toxicological impacts of mercury, as various natural processes in aquatic environments convert mercury into different inorganic and organic compounds. Notably, certain lower organisms can convert inorganic mercury into methylmercury, a compound known for its neurotoxic properties.[42–44] Given that the maximum allowable concentration in food and drinking water is around 2 ppb,[45] there is a strong interest in developing effective sensors for mercury detection. Various types of sensors have been developed that utilize electrochemical responses and conductivity changes,[46,47] as well as variations in color and fluorescence.[45,48–57] However, many of these sensors are limited to nonaqueous environments, and the direct detection of elemental mercury has primarily been conducted in its vapor form.[58,59] Therefore, sensors that can function in aqueous environments are of significant practical importance.

In our efforts to promote secure and healthy surroundings, we have concentrated on exploring straightforward methods for detecting and eliminating toxic substances from commonly affected areas. Various techniques have been utilized for the identification of $Hg^{2+}$, such as inductively coupled plasma mass spectrometry, surface-enhanced Raman spectroscopy, and atomic absorption spectrometry. However, these methods tend to be expensive, require extensive pre-treatment, and necessitate skilled personnel for operation.[60,61] Recently, there has been a surge of interest in colorimetric and fluorometric sensors for $Hg^{2+}$ ion detection, primarily due to their potential for miniaturization and suitability for field applications.[62–65] In this regard, fluorescent nanomaterial-based colorimetric sensors utilizing diverse functionalization techniques have significantly advanced the detection of $Hg^{2+}$ ions.[66–70] Nevertheless, most research has focused on detecting mercury ions in liquid solutions. At the same time, solid-state sensing methods are favored for practical, real-time applications due to their ease of handling, operational simplicity, stability, and portability.

Considering all relevant factors, we introduce an IL and IL-based organic nanosensor that incorporates the pyrene moiety. Through the reprecipitation technique, we developed water-dispersible crystalline nanoparticles that possess various important properties. Moreover, introducing $Hg^{2+}$ into the nNTIL solution results in a bathochromic shift of 2 nm (from 344 nm to 346 nm) and is accompanied by prominent Mie-scattering, inferring further coagulation of nNTIL. nNTIL demonstrated a substantial increase in fluorescence ($\phi$ = 0.37) when exposed to 365 nm UV light, making it readily observable compared with the NTIL solution. When mercury(II) ions were added to the nNTIL solution, a decrease in fluorescence was noticed at 478 nm ($\phi$ = 0.035). The quenching process is dynamic and is evident from the photoluminescence titration spectral and excited state lifetime decay analysis. The present report discusses the fabrication and implications of metal-sensitive IL-based nanoparticles that exhibit remarkable properties compared with traditional ones.

## 2. Experimental section

Information regarding the synthesis methods for NTIL and nNTIL, general protocols for conducting UV-visible and fluorescence analysis, determination of photoluminescence quantum yields, and various interactive plots are given in the ESI.†

### 2.1 Materials and instrumentations

For synthesizing pyrene butyrate anion-based NTIL, pyrene butyric acid (PBA), and trihexyltetradecylphosphonium chloride ($P_{66614}Cl$) (>95%) were purchased from Sigma-Aldrich, India. All the solvents used for the experiments were of analytical grade and obtained from Sigma-Aldrich, India, and TCI, India. All the metal chloride salts and Hg(II) anions used in the present study were purchased from Sigma-Aldrich, India, and TCI, India, respectively. All the chemicals were utilized without additional purification. $^1$H and $^{31}$P NMR spectra were recorded on a Bruker 400 MHz spectrometer in $CDCl_3$ with chemical shifts ($\delta$) in ppm units. $^{13}$C NMR spectra were recorded on a Bruker 100 MHz spectrometer in $CDCl_3$. FT-IR spectra were measured on a Bruker Optik GMBH FTIR spectrometer (Germany). High-resolution mass spectra (HRMS) were recorded on an Agilent 6545XT AdvanceBio LC/Q-TOF spectrometer. UV-visible spectral analysis was recorded on a Hitachi U-2910 instrument, and fluorometric experiments were performed using a Hitachi F-7100 fluorimeter. Throughout the steady state fluorometric experiment, excitation and emission wavelengths were kept at 330 nm and 340–650 nm, respectively, with 5 nm excitation and emission slit under ambient conditions and processed using Origin software.

The size and shape of nNTIL were estimated using field emission scanning electron microscopy (SEM) (ZEISS) employing an operating voltage of 50 kV by drop casting the required amounts of nNTIL (20 μg $mL^{-1}$) on the carbon-coated copper grids. The average particle size was determined considering the size of more than 100 particles. Transmission electron microscopy (JEOL TEM-2010) was used for determining the morphology of the nanoparticles with an operating voltage of 200 kV. The average particle size was obtained by measuring the size of more than 100 particles. The hydrodynamic radius of nNTIL was measured using the dynamic light scattering (DLS) technique (Malvern Zeta Sizer Nano) using a 4 mW He–Ne laser ($\lambda$ = 632.8 nm). Differential scanning calorimetry (DSC) experiment was carried out between 25 °C to 200 °C using a Perkin-Elmer aluminum sample pan kit in a PerkinElmer (DSC Q20) instrument at a scan rate of 2 °C $min^{-1}$ under a nitrogen atmosphere. Time-resolved fluorescence decays were obtained by using a picosecond time-correlated single-photon counting Life Spec II spectrophotometer (Edinburgh Instruments, UK). The decay profile was analyzed using F900 software from Edinburgh Instruments. For measuring the photoluminescence lifetime of nNTIL, samples were excited with 375 nm picosecond laser diodes (EPL-375) having an instrument response function (IRF) of ~260 ps. The signals were collected at a magic angle of 54.7°, monitoring the emission maxima at 480 nm. All of the fluorescence decays were fitted with a multiexponential function corresponding to a $\chi^2$ value close to 1, indicating a good fit. After deconvoluting the IRF, each decay curve was fitted with the help of the exponential decay function: $\tau(t) = \sum \alpha_i e^{-t/\tau_i}$, where $\alpha_i$ and $\tau_i$ values are the experimentally obtained pre-exponential factors having corresponding lifetimes. Experimentally as-obtained pre-exponential factors were then normalized by the equation $a_i = \frac{\alpha_i}{\sum \alpha_i}$ to achieve actual pre-exponential factors. The average photoluminescence lifetime was estimated utilizing the equation $\langle\tau\rangle = \frac{\sum a_i \tau_i}{\sum a_i}$ and percentage corresponding component were determined by employing $a_i \times 100$.

## 3. Results and discussion

### 3.1 Characterization of NTIL and nNTIL

Various spectroscopic techniques were employed to characterize the prepared NTIL. The results from $^1$H, $^{13}$C, and $^{31}$P NMR studies confirm that the ion-exchange reaction effectively yields NTIL (Fig. S1–S3, ESI†). In the high-resolution mass spectrometry (HRMS) analysis, a peak at 483.544 ($m/z$) corresponds to the cationic phosphonium moiety. In contrast, a peak at 287.104 ($m/z$) indicates the presence of the anionic pyrene butyrate moiety (Fig. S4, ESI†). The molecular weight of NTIL was calculated to be 770.648 Da from the equimolar mixing of the two oppositely charged components, and further confirms the synthesis of NTIL. The FT-IR spectrum revealed two bands associated with C–H stretching vibrations at 2927 and 2853 $cm^{-1}$, further supporting the development of NTIL (Fig. S5, ESI†). NTIL was observed to be a viscous solid at ambient temperature. To determine if the synthesized ionic salt can be classified as an ionic liquid, we carried out differential scanning calorimetry (DSC) analysis, which indicated a melting point of 69 °C (Fig. S6, ESI†), inferring that the synthesized organic salt belongs to the class of ionic liquids.

The UV-visible absorption spectrum of nNTIL displays a structured band that is notably broad and exhibits a bathochromic shift of approximately 6 nm relative to pyrene butyrate in solution (Fig. S7, ESI†). This redshift, along with significant Mie-scattering, represents the aggregation of pyrene moieties in the ground electronic state of water-suspended nNTIL. The presence of strong Mie-scattering suggests that the self-association of pyrene butyrate has led to the formation of water-suspended nanoparticles (Fig. 1(a)). nNTIL suspended in water displays a structured monomeric emission along with a broad, excimer-like emission characterized by high emission intensity displaying a cyan color photoluminosity. The cyan colored fluorogenicity from the water-suspended nanoparticles was observable even with minimal amounts of NTIL (Fig. 1(b)). The CIE diagrams for NTIL ($x$ = 0.1617, $y$ = 0.0368) and nNTIL ($x$ = 0.1403, $y$ = 0.2478) infer that these color co-ordinates values fall within the color gamut of blue and cyan color which are also visible to the naked eye under the exposure of a 365 nm UV lamp (Fig. 1(c)). The observation of a notably intense excimer-like emission implies that the pyrene molecules are closely

 

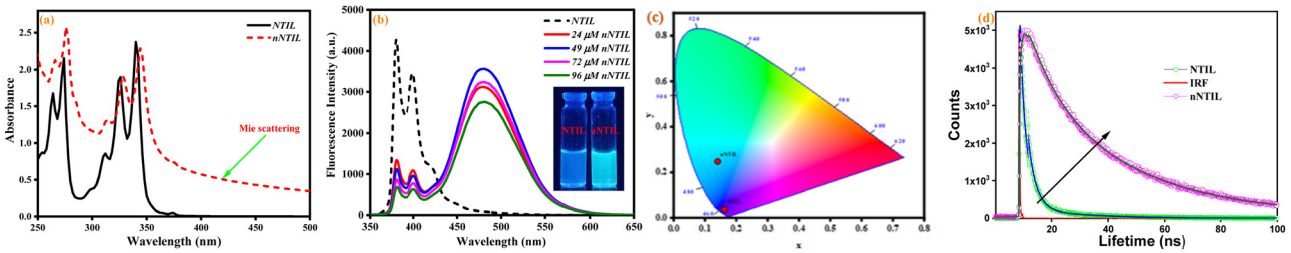


Fig. 1 (a) UV-visible absorption spectra of NTIL (49 μM) and nNTIL (49 μM). (b) Fluorescence spectra of NTIL and nNTIL in different amounts of NTIL. (c) CIE diagram of NTIL and nNTIL. (d) Photoluminescence lifetime decays of NTIL in THF and nNTIL in water.

stacked, resulting from substantial van der Waals interactions, leading to their pre-aggregation within the nanostructure. The presence of nanoparticles is validated by high-resolution dynamic light scattering (DLS) (Fig. 2(a)), SEM (Fig. 2(b)), transmission electron microscopy (HR-TEM) (Fig. 2(c)) analysis and energy dispersive X-ray spectroscopy (EDS) (Fig. S8, ESI†) and time-resolved photoluminescence decay analysis (Fig. 1(d)). The hydrodynamic radius was measured to be 410 ± 10 nm according to the DLS spectrum which was confirmed by SEM image analysis. The nNTIL nanoparticles suspended in water exhibit a spherical shape, suggesting the development of nanoballs. HR-TEM images also reveal that the nanoaggregates have a nearly spherical morphology, with an average size of 56 ± 5 nm. The melting point of the prepared nanoparticles was determined to be 153 °C, which was revealed from the observation of an exothermic peak during the heating process and associated with the melting temperature of ionic crystalline nNTIL as obtained from the differential scanning calorimetry (DSC) analysis (Fig. S9, ESI†). However, no exothermic peak was found in the cooling phase because of crystallization.

The excited-state photophysics of pyrene units within the nanoparticles was explored through time-resolved photoluminescence studies. In Birks' mechanism, the decay profile of the excimer is characterized by two components when preaggregation is absent.[71] The first is a rising component associated with the formation of the excited state dimer, which has a negative prefactor ($-a_1$). The second is a decaying component with a positive prefactor ($a_2$), which is linked to the deactivation process of the excimer. However, this mechanism may not be suitable for pre-aggregated systems, where there is a significant likelihood of associative pyrene dimer formation in the ground state. In these systems, a substantial portion of the excimer originates from the pre-aggregated dimers. This means that the rising component should be detectable on a very short timescale, specifically within 1 nanosecond.[72] Time-resolved fluorescence measurements reveal that the decay profile of the excited species of nNTIL observed at the excimer-like emission exhibits a very short rise time accompanied by long decay components. The rising component has a lifetime of less than 1 nanosecond, which is significantly faster than that of pyrene excimers in bulk solvent. These results strongly suggest that the pyrene moieties are situated in an environment that enhances their association in the excited electronic state, leading to a much quicker formation of the excited state complex compared with what is observed in bulk solvents. In contrast to the concept of excited state dimerization, one could contend that a significant association of multiple pyrene moieties occurs in the excited state rather than solely the formation of dimers within the synthesized nanoparticle system. For NTIL in THF solution, time-resolved photoluminescence decay shows three exponential profiles, with lifetimes of $\tau_1$ = 0.555 ns (36%), $\tau_2$ = 2.819 ns (60%), and $\tau_3$ = 35.567 ns (4%) inferring that the faster, moderate and long lifetime components are likely excimeric, pre-aggregated and aggregated pyrene moieties ones. The excited state lifetime decay profile of nNTIL is characterized by a triexponential profile, with lifetimes of $\tau_1$ = 1.160 ns (−29%), $\tau_2$ = 10.006 ns (41%), and $\tau_3$ = 35.567 ns (88%), inferring that rise, moderate and long lifetime components are for the excimeric, pre-aggregated and aggregated pyrene moieties, respectively, and most of the pyrene moieties are stacked in aggregated states. The average fluorescence lifetime ($\langle\tau\rangle$) yields a lifetime of 35.284 ns for the aggregated pyrene (88%) in water-suspended nanoparticles, while the average photoluminescence lifetime of NTIL in THF is 2.682 ns, with

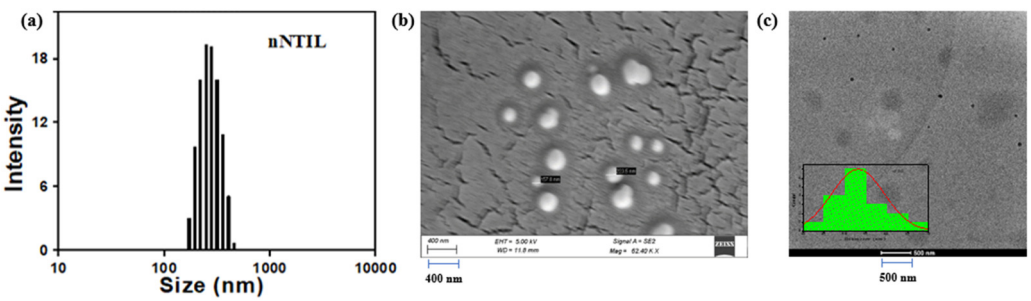


Fig. 2 (a) DLS spectrum, (b) SEM, and (c) HR-TEM images of the fabricated nNTIL.

Table 1 The parameters for time-resolved fluorescence lifetime decay along with the average fluorescence lifetime of NTIL in THF and nNTIL in water at excitation and emission wavelengths of 375 nm and 480 nm, respectively

| | $a_1$[a] | $\tau_1$[b] (ns) | $a_2$[a] | $\tau_2$[b] (ns) | $a_3$[a] | $\tau_3$[b] (ns) | $\langle\tau\rangle$[c] (ns) | $\chi^2$[d] |
|---|---|---|---|---|---|---|---|---|
| NTIL | 0.36 | 0.555 | 0.60 | 2.819 | 0.04 | 21.135 | 2.682 | 1.15 |
| nNTIL | −0.29 | 1.160 | 0.41 | 10.006 | 0.88 | 35.567 | 35.284 | 1.08 |

[a] Denotes the pre-exponential factors. [b] $\tau_1$, $\tau_2$, and $\tau_3$ are in ns. [c] Indicates average fluorescence lifetime. [d] Represents the parameters indicating the goodness of fit.

only 4% pyrene moieties in the aggregated state (Fig. 1(d) and Table 1).

### 3.2 Spectroscopic response of nNTIL towards metal ions

The absorption characteristics of nNTIL were evaluated using UV-visible spectroscopy in an aqueous environment. The UV-visible absorption spectrum of nNTIL displays a structured band that is notably broad and exhibits a bathochromic shift of approximately 6 nm relative to pyrene butyrate in solution (Fig. S7, ESI†). This redshift, along with significant Mie-scattering, represents the aggregation of pyrene moieties in the ground electronic state of the water-suspended nNTIL. The presence of strong Mie-scattering suggests that the self-association of pyrene butyrate has led to the formation of nanoparticles that are suspended in water. Furthermore, the UV-visible spectra of the synthesized nNTIL nanoparticles show a marked change in absorption upon the addition of $Hg^{2+}$ ions (Fig. 3(a)). Specifically, introducing $Hg^{2+}$ into the nNTIL solution results in a bathochromic shift of 2 nm (from 344 nm to 346 nm) and is accompanied by prominent Mie-scattering. The long-wavelength tail observed in the absorption spectrum of the nanoparticle suspension is attributed to $\lambda^{-4}$ Rayleigh-type scattering.[73] The observation of a greater bathochromic shift and prominent Mie-scattering in the presence of $Hg^{2+}$ ions indicate the further association of pyrene moieties inside the crystalline nanoball due to the strong electrostatic interaction among pyrene butyrate and $Hg^{2+}$ ions. However, we have found no change in the absorption spectra with the addition of $Hg^{2+}$ in NTIL solution (Fig. S10, ESI†). Furthermore, titration of aqueous $Hg^{2+}$ solution with nNTIL at different concentrations showed significant Mie-scattering (Fig. S11, ESI†).

To better understand the binding characteristics of nNTIL towards $Hg^{2+}$ ions, fluorescence titration experiments were performed. nNTIL exhibited remarkable sensitivity to $Hg^{2+}$ ions among the various metal ions examined. The probe demonstrated a significantly enhanced cyan color fluorescence ($\phi$ = 0.37) under 365 nm UV light, which is easily observable to the naked eye. Upon the addition of $Hg^{2+}$ ions to the probe solution, cyan color fluorescence quenching was observed at 478 nm ($\phi$ = 0.035) (Fig. 3(b) and (c)), which is also evident from the CIE diagram (Fig. 3(d)). The coordinate values for nNTIL are $x$ = 0.1402 and $y$ = 0.2416. In the case of nNTIL-$Hg^{2+}$, the coordinate values are $x$ = 0.1485 and $y$ = 0.1839. Thus, nNTIL acts as an effective ''turn-off'' sensor for the detection of $Hg^{2+}$ ions. However, there is no obvious change in fluorescence intensity with the addition of $Hg^{2+}$ in NTIL solution (Fig. S12, ESI†). The quenching effect of the probe increased progressively with rising concentrations of $Hg^{2+}$ ions from 0 to 113 μM. Utilizing the fluorometric titration data and applying the $3\sigma/K$ and $10\sigma/K$ methods, we estimated the limit of detection (LOD) and quantification (LOQ) for $Hg^{2+}$ ions.[74] In this context, $\sigma$ denotes the standard deviation of the blank, while $K$ represents the slope of the calibration curve. A robust linear correlation between fluorescence intensity and $Hg^{2+}$ ions concentration was established in two ranges: 5 μM to 30 μM and 60 μM to 120 μM, yielding $R^2$ values of 0.96 and 0.98, respectively. The LOD and LOQ for $Hg^{2+}$ were estimated to be 17 nM and 57 nM, respectively (Fig. S13a, ESI†), which is considerably lower than those reported in earlier studies (Table S2, ESI†). $Hg^{2+}$ ions are inclined to bind with the carboxyl groups of nNTIL; however, this interaction is expected to be weak, as 'soft' $Hg^{2+}$ ions favor a 'soft' coordination environment. These results suggest that the quenching response of the sensor is primarily due to the strong π–π stacking interactions among the pyrene moieties inside the crystalline nanoball owing to the pronounced electrostatic interaction among pyrene butyrate and $Hg^{2+}$ ions. The association constant is determined to be $0.55 \times 10^5$ $M^{-1}$ using the Benesi–Hildebrand equation[75] (Fig. S13b, ESI†).

To validate the suggested mechanism, the size distribution of particles with the addition of $Hg^{2+}$ ions is measured by DLS (Fig. S14, ESI†). The DLS spectrum of free nNTIL shows that the hydrodynamic diameter of the nanoparticles suspended in water falls within the range of 410 ± 10 nm, but the hydrodynamic diameter of the aqueous suspended nanoparticles is in the range of 320 ± 10 nm after the addition of $Hg^{2+}$. The decrease in hydrodynamic radius might be due to the removal of bonded water from the core of nNTIL due to the further $Hg^{2+}$-induced clotting of NTIL. Also, the DLS spectrum of NTIL-$Hg^{2+}$ lies in a broader size range than NTIL. Therefore, there is coagulation of nano-particles after the addition of $Hg^{2+}$. From the SEM images of nNTIL-$Hg^{2+}$ (Fig. S15, ESI†), we can conclude that more aggregation is pronounced when $Hg^{2+}$ is present inside the crystalline nanoball, which is also observed in the UV-visible spectral studies (Fig. 3(a)). Also, the presence of $Hg^{2+}$ is evident from the EDS analysis. EDS results show that only three components are present in nNTIL (C, O, and P) (Fig. S8, ESI†), while four components are present in nNTIL-$Hg^{2+}$: C, O, P, and Hg (Fig. S16, ESI†).

To assess the selectivity of nNTIL for $Hg^{2+}$ and to explore the mechanistic details of its detection, time-resolved photoluminescence decay analysis was conducted. Fig. 4 shows the excited-state photoluminescence lifetime decay of nNTIL with and without $Hg^{2+}$ (various $Hg^{2+}$ ion concentrations at a 375 nm

 

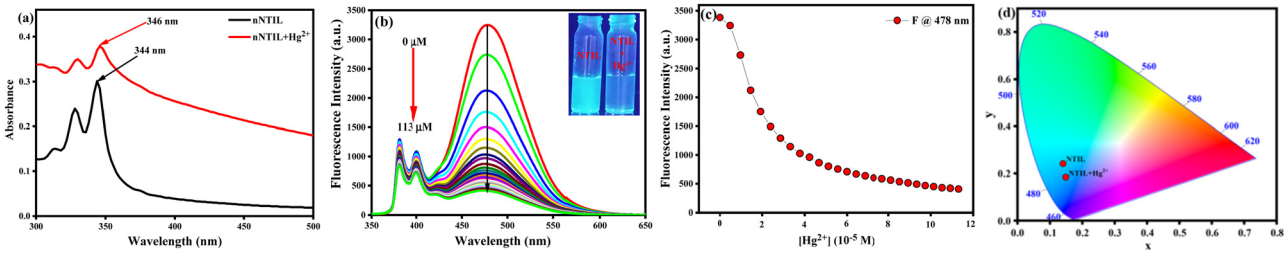


Fig. 3 (a) Absorption spectra of nNTIL (49 μM) with and without $Hg^{2+}$ ions in water. (b) Photoluminescence titration spectra of nNTIL (49 μM), $\lambda_{exc}$ = 330 nm (slit = 5 nm), showing the response to different concentrations of $Hg^{2+}$ (0–113 μM). (c) Corresponding variations in emission intensity at 478 nm resulting from the inclusion of $Hg^{2+}$ (113 μM) into the nNTIL (49 μM) solution. (d) CIE diagram illustrating the color coordinates for nNTIL (49 μM) and nNTIL-$Hg^{2+}$.

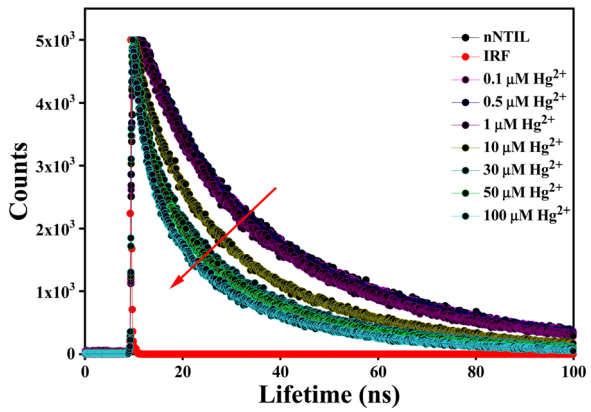


Fig. 4 Photoluminescence lifetime decays of nNTIL in water with and without $Hg^{2+}$ ions at various concentrations. $\lambda_{exc.}$ = 375 nm.

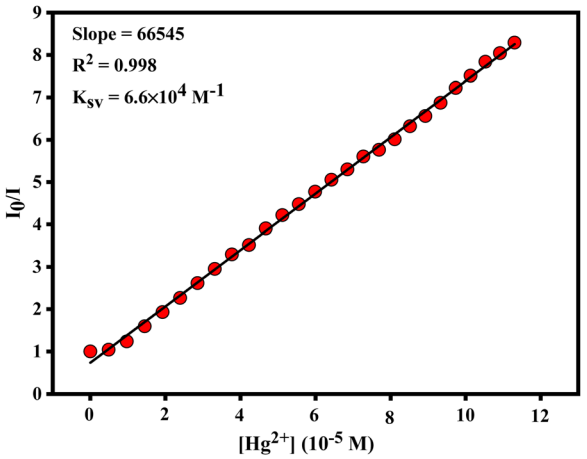


Fig. 5 Stern–Volmer plot for the determination of the quenching constant.

excitation wavelength). Remarkably, the average fluorescence lifetime ($\langle\tau\rangle$) of nNTIL is exceptionally diminished with the inclusion of $Hg^{2+}$ ions, and the average lifetime diminished from 35.284 ns to 11.117 ns at $\lambda_{exc}$ = 375 nm when $Hg^{2+}$ is present (Table 2).

The fluorescence emission of nNTIL exhibits quenching behavior in response to varying concentrations of $Hg^{2+}$ ions, adhering to the Stern–Volmer relationship:

$$\left(\frac{F_0}{F}\right) = 1 + K_{sv}[Q]$$

where $F_0$ and $F$ represent the emission intensities of nNTIL with or without $Hg^{2+}$ ions, respectively; the Stern–Volmer quenching constant is denoted as $K_{SV}$, and [Q] is the concentration of $Hg^{2+}$ ions. The substantial Stern–Volmer quenching constant [$K_{SV}$ = $6.6 \times 10^4$ $M^{-1}$] implies a potential for long-range dipole–dipole interactions of nNTIL with $Hg^{2+}$ ions[28,76] (Fig. 5). The sensor's performance is closely linked to how it functions. This system relies on dynamic quenching, where a quencher interacts with a molecule in its excited state. Consequently, the sensor's

Table 2 The parameters for time-resolved fluorescence lifetime decay along with the average fluorescence lifetime of nNTIL at 375 nm with and without various aliquots of $Hg^{2+}$ ions

| [$Hg^{2+}$] (μM) | $a_1$ [a] | $\tau_1$ [b] (ns) | $a_2$ [a] | $\tau_2$ [b] (ns) | $a_3$ [a] | $\tau_3$ [b] (ns) | $\langle\tau\rangle$ [c] (ns) | $\chi^2$ [d] |
|---|---|---|---|---|---|---|---|---|
| 0 | −0.29 | 1.160 | 0.41 | 10.006 | 0.88 | 35.567 | 35.284 | 1.08 |
| 0.1 | −0.21 | 1.441 | 0.39 | 10.237 | 0.82 | 35.444 | 32.663 | 1.03 |
| 0.5 | −0.14 | 1.519 | 0.37 | 10.693 | 0.77 | 35.381 | 31.128 | 1.04 |
| 1 | −0.14 | 1.408 | 0.38 | 9.940 | 0.76 | 34.173 | 29.619 | 1.04 |
| 10 | 0.14 | 1.424 | 0.35 | 9.469 | 0.51 | 29.921 | 18.721 | 1.15 |
| 30 | 0.26 | 1.301 | 0.35 | 8.313 | 0.39 | 27.914 | 14.136 | 1.08 |
| 50 | 0.33 | 1.710 | 0.34 | 9.163 | 0.33 | 27.812 | 12.942 | 1.16 |
| 100 | 0.37 | 1.439 | 0.34 | 8.428 | 0.29 | 26.818 | 11.117 | 1.1 |

[a] Denotes the pre-exponential factors. [b] $\tau_1$, $\tau_2$, and $\tau_3$ are in ns. [c] Indicates average fluorescence lifetime. [d] Represents the parameters indicating the goodness of fit.

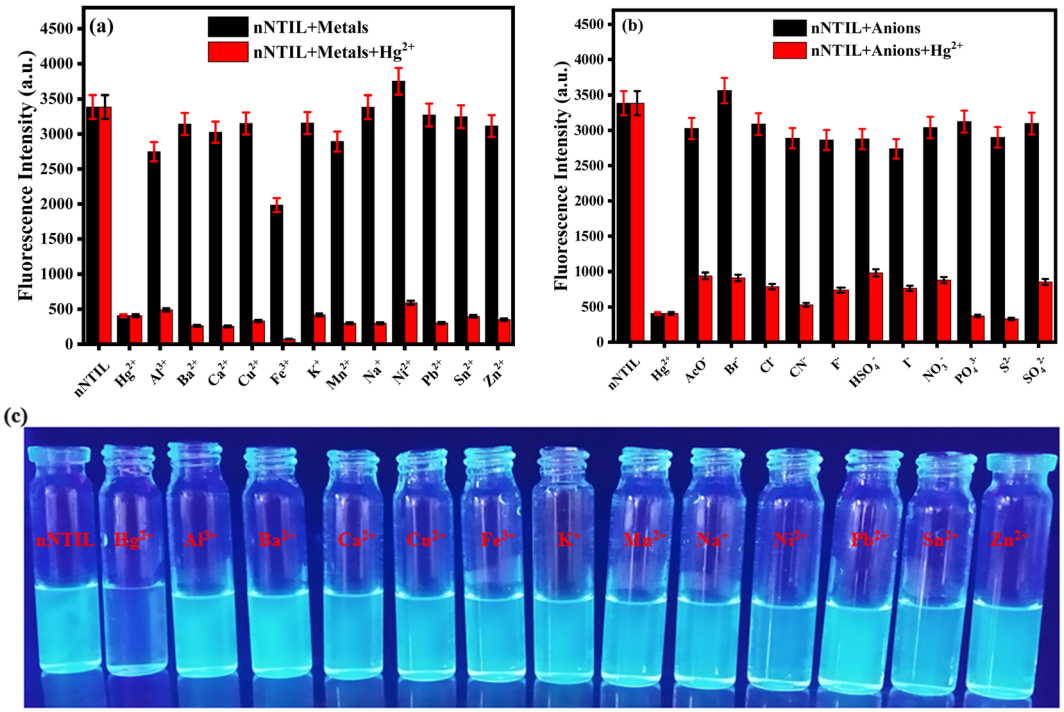


Fig. 6 Analysis of the interaction of nNTIL (49 μM) with $Hg^{2+}$ (113 μM) alongside different (a) metal ions (113 μM) and (b) anions (113 μM). $\lambda_{exc}$ = 330 nm, and $\lambda_{emi}$ = 340 nm. (c) Photograph showing the selectivity of nNTIL (49 μM) towards various metal ions (113 μM).

sensitivity is heavily influenced by the excited state lifetime from which the emitted fluorescence originates.[28] Therefore, the extended fluorescence lifetime observed in this sensor is advantageous for ensuring an effective sensing process, particularly when the mechanism of action involves dynamic quenching.

### 3.4 Fluorescence behavior of nNTIL in response to various cations and anions

A key aspect in assessing the performance of a chemical sensor is its high selectivity for the probe nNTIL compared with other competing species present in the sample. We investigated the selectivity of nNTIL towards different cations: $Hg^{2+}$, $Sn^{2+}$, $Zn^{2+}$, $Cu^{2+}$, $Mn^{2+}$, $Ni^{2+}$, $K^{+}$, $Na^{+}$, $Pb^{2+}$, $Al^{3+}$, $Ba^{2+}$, $Ca^{2+}$ and $Fe^{3+}$. The nNTIL probe solution exhibits cyan fluorescence and the presence of these metal ions did not affect the fluorescence properties of the probe (Fig. 6(c)). However, $Hg^{2+}$ ions quench the cyan fluorescence when examined under a UV lamp with an excitation wavelength of 365 nm. Additionally, we assessed the selectivity of the probe against a range of anions: $AcO^{-}$, $Br^{-}$, $Cl^{-}$, $CN^{-}$, $F^{-}$, $HSO_4^{-}$, $I^{-}$, $NO_3^{-}$, $PO_4^{3-}$, $S^{2-}$, and $SO_4^{2-}$. The minimal interference from different competing metal ions and anions highlights the exceptional selectivity of the sensor toward $Hg^{2+}$ ions in aqueous solutions.

To confirm the strong selectivity for $Hg^{2+}$ amidst a complex mixture of various cations in an aqueous medium, we examined the fluorescence intensity quenching of nNTIL in the presence of $Hg^{2+}$ ions when different competing cations and anions are present. $Hg^{2+}$ at 113 μM was introduced into the probe solution alongside various metal ions and anions. The quenching of photoluminescence intensity due to the presence of $Hg^{2+}$ ions remained consistent, even after the inclusion of various cations and anions (Fig. 6(a) and (b)). Notably, the added cations and anions did not affect the detection of $Hg^{2+}$ ions when equivalent amounts were present in the probe solution. This indicates that the nNTIL probe is likely to function effectively *in vivo*, despite the presence of other competing ions. Overall, these findings demonstrate that the specified ions do not notably hinder the identification of $Hg^{2+}$ ions by nNTIL.

## 4. Analysis in real water and soil samples

Sensing systems that facilitate the detection of trace metal ions in both real and spiked samples have gained considerable interest.[49,50] To assess the practicality of the proposed method, a study was conducted to detect $Hg^{2+}$ ions in actual water samples collected from Siliguri, West Bengal. All samples were spiked with $Hg^{2+}$ ions. The quantitative recovery results were obtained from these spiked samples using a calibration curve for the calculations. The recovery rates for $Hg^{2+}$ in the water samples were between 98% and 99% (Table S1, ESI†). These findings demonstrate that the nNTIL probe is capable of accurately and precisely detecting $Hg^{2+}$ in environmental analyses.

Mercury is notoriously resistant to degradation and tends to accumulate in crops and soil, making its quantitative detection in soil crucial. In this investigation, we employed the nNTIL

 

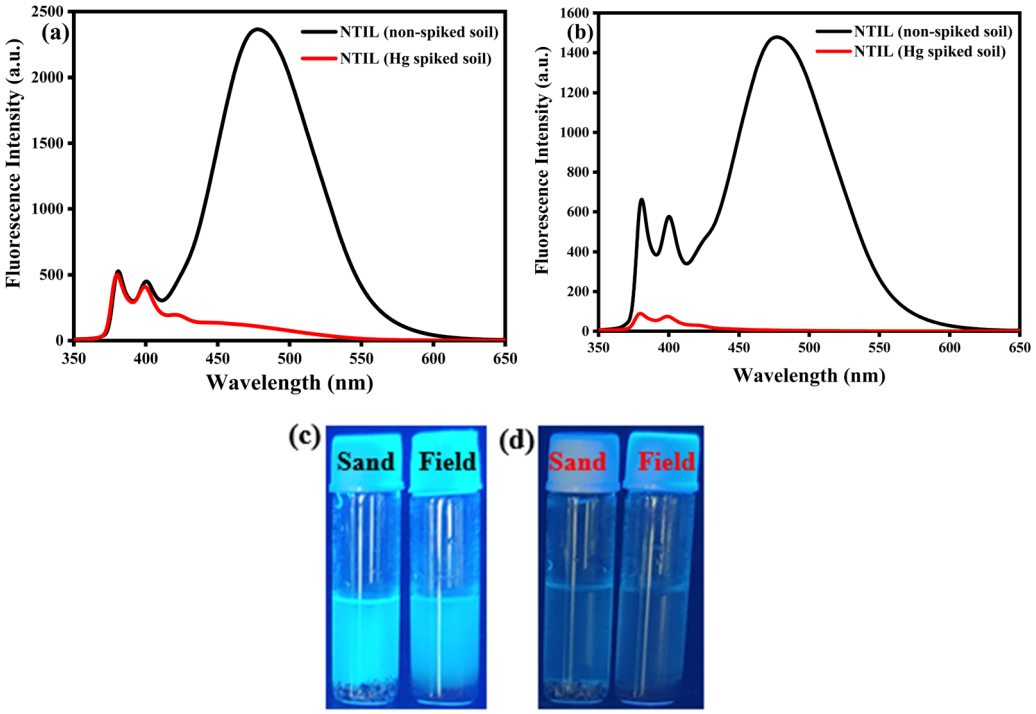


Fig. 7 (a) Variations in fluorescence intensity observed in sandy soil. (b) Variations in fluorescence intensity observed in field soil. (c) Images of nNTIL (49 μM) without spiking soil samples with $Hg^{2+}$. (d) Images of nNTIL (49 μM) when the soil samples were spiked with $Hg^{2+}$ ions ($10^{-2}$ M).

probe to measure mercury levels in soil samples sourced from Siliguri, West Bengal. Each sample was initially weighed at 0.5 g. The fluorescent sensor was first used to analyze the unspiked samples. Following this, all samples were spiked with $Hg^{2+}$ and re-evaluated using the developed fluorescent sensor. The results indicated that the unspiked sandy soil produced a strong cyan fluorescence, while the field soil showed a lower intensity of fluorescence under UV light (365 nm). After spiking with $Hg^{2+}$, both soil types exhibited a significant reduction in cyan fluorescence (Fig. 7(a)–(d)). These results demonstrate the potential

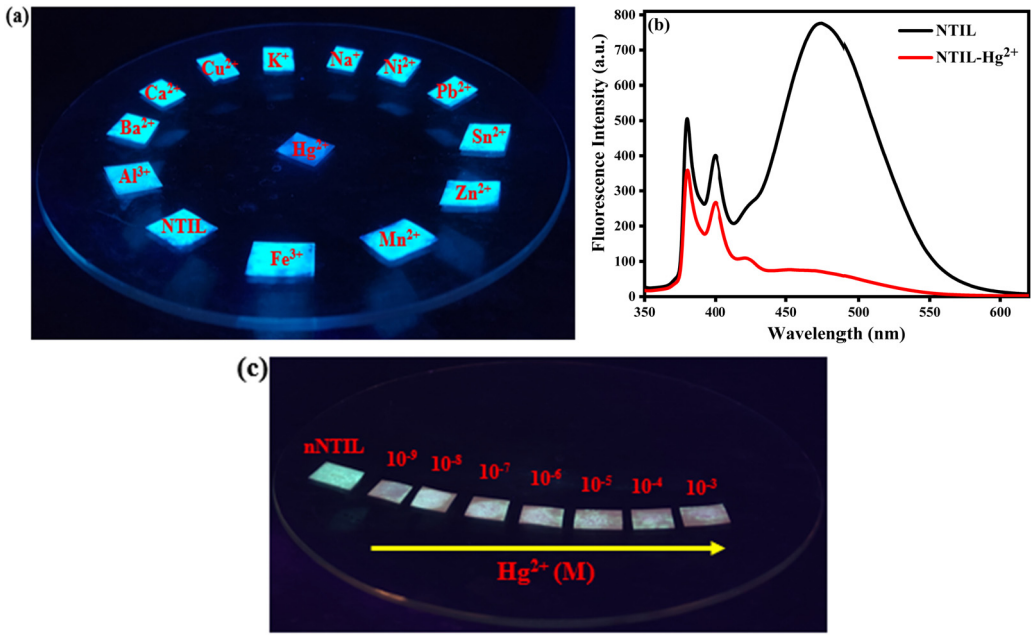


Fig. 8 (a) Images of test strips after being immersed in nNTIL (49 μM) alongside various metal ions ($10^{-2}$ M) used in the selectivity experiment. (b) Changes in the fluorescent intensity of the paper strip with and without $Hg^{2+}$ ions ($10^{-2}$ M). (c) An illustrative photograph depicting nNTIL-coated paper strips after being exposed to varying concentrations of $Hg^{2+}$ ions ($10^{-3}$–$10^{-9}$ M) when illuminated by a 365 nm UV lamp.

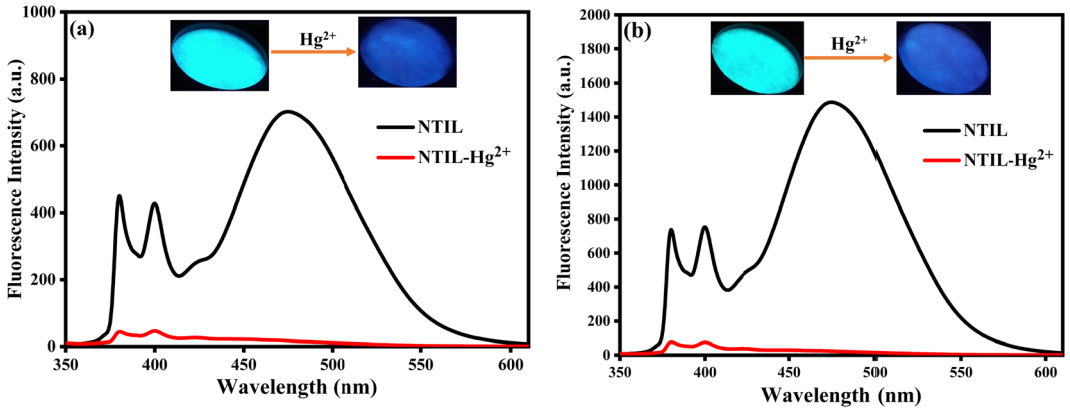


Fig. 9 (a) Fluorescent intensity and color variations of the paper strip with and without $Hg^{2+}$ ions ($10^{-2}$ M) in municipal water. (b) Fluorescent intensity and color variations of the paper strip with and without $Hg^{2+}$ ions ($10^{-2}$ M) in tap water.

of the nNTIL probe for effectively detecting mercury in environmental materials, especially in water and soil samples.

## 5. Sensing with test strips

To assess the sensing characteristics of the probe for mercury(II) ions in aqueous solutions, we performed experiments using test strips for practical applications. These strips were prepared by soaking them in an nNTIL solution, followed by the addition of different metal ion solutions. Afterward, the strips were allowed to dry at room temperature. The results indicated that the cyan fluorescence of the test strip only diminished in the presence of mercury when irradiated at 365 nm (Fig. 8(a) and (b)). Furthermore, we conducted a real sample analysis using the paper strip method to confirm its applicability in real-time settings. In this process, the nNTIL-coated paper strip was dipped into various water samples containing $Hg^{2+}$ ions, including municipal and tap water from Siliguri, West Bengal, and subsequently dried in an oven. Notably, the dried strips exhibited a quenching of cyan fluorescence, indicating the presence of $Hg^{2+}$ ions (Fig. 9(a) and (b)). We conducted a detailed investigation into the concentration-dependent response of nNTIL-coated paper strips to $Hg^{2+}$ ions, aiming to illustrate their ability to quantify $Hg^{2+}$ ions. The experiment was carried out across a range of $Hg^{2+}$ ions concentrations, from $10^{-1}$ to $10^{-9}$. The cyan fluorescence of the nNTIL-coated paper strips was quenched (Fig. 8(c)). The effective use of affordable test strip techniques and their application in different water samples demonstrate the probe's potential for detecting and quantifying mercury(II) ions in real sample analysis.

## 6. Utilization of neat NTIL for the identification of $Hg^{2+}$ ions

Neat NTIL displays a broad fluorescence band at 478 nm, producing a bright cyan fluorescence when illuminated with

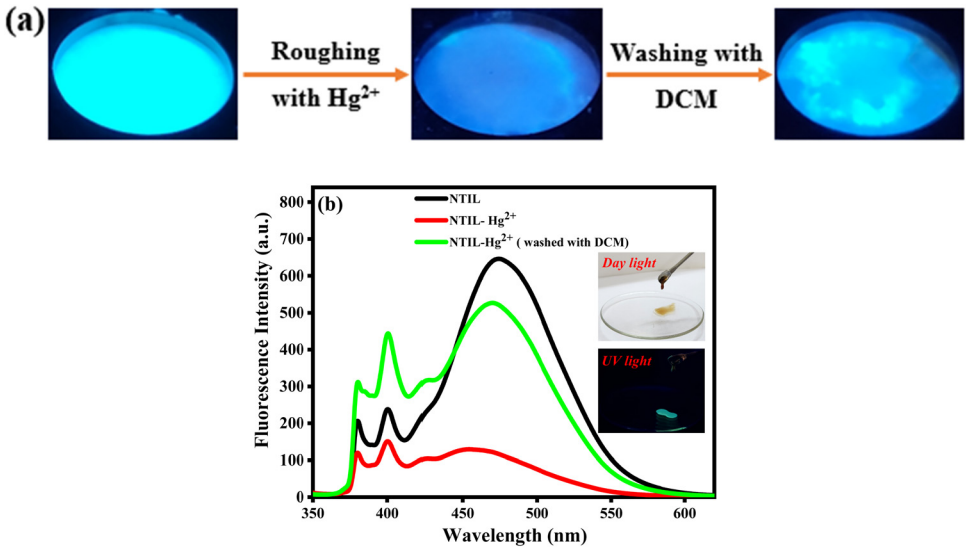


Fig. 10 (a) Photoluminescence characteristics of neat NTIL-loaded filter paper after roughening with $Hg^{2+}$ ions and its restoration following DCM washing. (b) Changes in the fluorescence intensity of the pure NTIL-loaded filter paper following treatment with mercury and its restoration after being washed with DCM. Inset: Images of neat NTIL in daylight and under UV light.

 

a 365 nm UV lamp. This luminescence nearly disappears upon the introduction of mercury, with the intensity at 478 nm almost decreasing, indicating its capability to detect trace levels of $Hg^{2+}$ ions. The fluorescence characteristics of the NTIL-loaded filter paper and its quenching effect upon the addition of $Hg^{2+}$ ions in solution under 365 nm UV light are illustrated in Fig. 10(a) and (b). A crucial feature of any detection system is its ability to restore functionality after use. To address this, we aimed to recover the cyan fluorescence of NTIL-loaded filter paper. After washing the NTIL-loaded filter paper with DCM and drying it under vacuum conditions, there was a partial recovery of fluorescence (Fig. 10(a) and (b)).

## 7. Conclusion

The present report introduces a pyrene butyrate-based ionic liquid (NTIL) and its low dimensional material, nNTIL, for the selective and sensitive identification of $Hg^{2+}$ ions. In an aqueous environment, NTIL generates nanoparticles that possess various important photophysical properties. Within these nanomaterials (referred to as nanoballs), the pyrene units are arranged in a crystalline lattice structure. The nanocrystallinity within the nanoparticles was investigated using steady-state and time-resolved spectroscopy, microscopy, and calorimetric techniques. These nanoparticles demonstrate a unique excited state association of luminogens, where the chromophore units further aggregate in their first excited electronic state, exhibiting behavior that goes beyond mere dimerization. Moreover, introducing $Hg^{2+}$ into the nNTIL solution results in a bathochromic shift of 2 nm (from 344 nm to 346 nm). It is accompanied by prominent Mie-scattering, inferring further aggregation due to the strong electrostatic interaction between pyrene butyrate and $Hg^{2+}$ ions, resulting in a remarkable quenching of photoluminosity of nNTIL. The quenching process is dynamic due to strong π–π stacking interactions among the pyrene moieties due to enhanced electrostatic interactions between pyrene butyrate and $Hg^{2+}$ ions. The enhanced electrostatic interaction between pyrene butyrate and $Hg^{2+}$ ions causes the congealing of nanoparticles, which is revealed from SEM analysis. The EDS results further corroborate the presence of $Hg^{2+}$ ions within the coagulated crystalline nanomaterials. The quenching process is also evident from the photoluminescence lifetime decay analysis. The practical applications of this sensor were illustrated through analysing water and soil samples, paving the way for further applications in diverse fields. Furthermore, we investigated the sensor's effectiveness in detecting mercury(II) ions using affordable test strips. Also, neat NTIL can identify $Hg^{2+}$ ions and restore the cyan fluorescence of NTIL by washing with DCM using these cost-effective strips.

## Data availability

The data supporting this article have been included as part of the ESI.†

## Conflicts of interest

There are no conflicts of interest to declare.

## Acknowledgements

We thank the Anusandhan National Research Foundation (ANRF) erstwhile Science and Engineering Research Board (SERB), New Delhi, Govt. of India, (Grant No: EEQ/2023/000048) for the financial support; the Ministry of Minority Affairs for the Maulana Azad National Fellowship awarded to NT; and the Govt. of West Bengal, India, for the Swami Vivekananda Merit Cum Means Scholarship provided to SA, JC, and MM, respectively. We are indebted to Prof. Mintu Halder, Indian Institute of Technology, Kharagpur, for allowing us to record time-resolved fluorescence decay profiles in their TCSPC set-up.

## References

1 J. Burke, A taste of the future, *Nat. Mater.*, 2003, **2**, 363–365.
2 J. P. Hallett and T. Welton, Room-temperature ionic liquids: Solvents for synthesis and catalysis. 2, *Chem. Rev.*, 2011, **111**, 3508–3576.
3 N. V. Plechkova and K. R. Seddon, Applications of ionic liquids in the chemical industry, *Chem. Soc. Rev.*, 2007, **37**, 123–150.
4 P. Kipkorir and S. Magut, *Ionic Liquids and GUMBOS for Biomedical and Sensing Applications*, PhD thesis, Louisiana State University, 2014.
5 D. R. Macfarlane, N. Tachikawa, M. Forsyth, J. M. Pringle, P. C. Howlett, G. D. Elliott, J. H. Davis, M. Watanabe, P. Simon and C. A. Angell, Energy applications of ionic liquids, *Energy Environ. Sci.*, 2013, **7**, 232–250.
6 M. Smiglak, A. Metlen and R. D. Rogers, The second evolution of ionic liquids: from solvents and separations to advanced materials–energetic examples from the ionic liquid cookbook, *Acc. Chem. Res.*, 2007, **40**, 1182–1192.
7 M. Smiglak, J. M. Pringle, X. Lu, L. Han, S. Zhang, H. Gao, D. R. Mac Farlane and R. D. Rogers, Ionic liquids for energy, materials, and medicine, *Chem. Commun.*, 2014, **50**, 9228–9250.
8 S. Zhang, K. Dokko and M. Watanabe, Porous ionic liquids: synthesis and application, *Chem. Sci.*, 2015, **6**, 3684–3691.
9 S. Zhang, K. Dokko and M. Watanabe, Carbon materialization of ionic liquids: from solvents to materials, *Mater. Horiz.*, 2015, **2**, 168–197.
10 S. Zhang, Q. Zhang, Y. Zhang, Z. Chen, M. Watanabe and Y. Deng, Beyond solvents and electrolytes: Ionic liquids-based advanced functional materials, *Prog. Mater. Sci.*, 2016, **77**, 80–124.
11 J. Liang, M. Chu, Z. Zhou, Y. Yan and Y. S. Zhao, Optically Pumped Lasing in Microscale Light-Emitting Electrochemical Cell Arrays for Multicolor Displays, *Nano Lett.*, 2020, **20**, 7116–7122.

12 J. Cui, Y. Li, D. Chen, T.-G. Zhan, K.-D. Zhang, J. Cui, Y. Li, T.-G. K. Zhan, D. Zhang and D. Chen, Ionic Liquid-Based Stimuli-Responsive Functional Materials, *Adv. Funct. Mater.*, 2020, **30**, 2005522.
13 Y. Yoshida and H. Kitagawa, Chromic Ionic Liquids, *ACS Appl. Electron. Mater.*, 2021, **3**, 2468–2482.
14 W. I. S. Galpothdeniya, F. R. Fronczek, M. Cong, N. Bhattarai, N. Siraj and I. M. Warner, Tunable GUMBOS-based sensor array for label-free detection and discrimination of proteins, *J. Mater. Chem. B*, 2016, **4**, 1414–1422.
15 K. S. Egorova, E. G. Gordeev and V. P. Ananikov, Biological Activity of Ionic Liquids and Their Application in Pharmaceutics and Medicine, *Chem. Rev.*, 2017, **117**, 7132–7189.
16 Z. Rahman and S. K. Das, Ionic Liquids based Acid-base Indicators for Aqueous to the Non-Aqueous Medium: An Overview, *ChemistrySelect*, 2021, **6**, 9164–9174.
17 Z. Rahman and S. K. Das, Ionic-Liquid-Based, Sustainable Wavelength-Shifting Materials for Energy Conversion: A Minireview, *ChemistrySelect*, 2022, **7**, e202103898.
18 M. Mahato, Y. Murakami and S. K. Das, Recent advances and applications of ionic liquids-based photonic materials, *Appl. Mater. Today*, 2023, **32**, 101808.
19 C. N. R. Rao and A. K. Cheetham, Science and technology of nanomaterials: current status and future prospects, *J. Mater. Chem.*, 2001, **11**, 2887–2894.
20 S. Kayal, A. Mandal, P. Pramanik and M. Halder, Hypothesizing the applicability of the principle of linear combination in predicting sensing behaviors of quantum dots: A deeper understanding of the precise tuning of quantum dot properties with capping composition, *J. Photochem. Photobiol., A*, 2019, **373**, 182–190.
21 G. Sahay, J. O. Kim, A. V. Kabanov and T. K. Bronich, The exploitation of differential endocytic pathways in normal and tumor cells in the selective targeting of nanoparticulate chemotherapeutic agents, *Biomaterials*, 2010, **31**, 923–933.
22 K. S. Egorova, E. G. Gordeev and V. P. Ananikov, Biological Activity of Ionic Liquids and Their Application in Pharmaceutics and Medicine, *Chem. Rev.*, 2017, **117**, 7132–7189.
23 M. Galluzzi, S. Bovio, P. Milani and A. Podestà, Surface Confinement Induces the Formation of Solid-Like Insulating Ionic Liquid Nanostructures, *J. Phys. Chem. C*, 2018, **122**, 7934–7944.
24 M. Antonietti, D. Kuang, B. Smarsly and Y. Zhou, Ionic Liquids for the Convenient Synthesis of Functional Nanoparticles and Other Inorganic Nanostructures, *Angew. Chem., Int. Ed.*, 2004, **43**, 4988–4992.
25 J. Z. Du, X. J. Du, C. Q. Mao and J. Wang, Tailor-Made dual pH-sensitive polymer-doxorubicin nanoparticles for efficient anticancer drug delivery, *J. Am. Chem. Soc.*, 2011, **133**, 17560–17563.
26 H. Kasai, T. Murakami, Y. Ikuta, Y. Koseki, K. Baba, H. Oikawa, H. Nakanishi, M. Okada, M. Shoji, M. Ueda, H. Imahori and M. Hashida, Creation of Pure Nanodrugs and Their Anticancer Properties, *Angew. Chem., Int. Ed.*, 2012, **51**, 10315–10318.
27 F. Winnik, Photophysics of Preassociated Pyrenes in Aqueous Polymer Solutions and in Other Organized Media, *Chem. Rev.*, 1993, **93**, 587–614.
28 J. R. Lakowicz, Principles of fluorescence spectroscopy, *Principles of Fluorescence Spectroscopy*, 2006, pp. 1–954.
29 Q. Dai, W. Liu, X. Zhuang, J. Wu, H. Zhang and P. Wang, Ratiometric fluorescence sensor based on a pyrene derivative and quantification detection of heparin in aqueous solution and serum, *Anal. Chem.*, 2011, **83**, 6559–6564.
30 G. Sivaraman, T. Anand and D. Chellappa, Development of a pyrene based '' turn on'' fluorescent chemosensor for $Hg^{2+}$, *RSC Adv.*, 2012, **2**, 10605–10609.
31 H. Tong, Y. Hong, Y. Dong, M. Häussler, Z. Li, J. W. Y. Lam, Y. Dong, H. H. Y. Sung, I. D. Williams and B. Z. Tang, Protein detection and quantitation by tetraphenylethene-based fluorescent probes with aggregation-induced emission characteristics, *J. Phys. Chem. B*, 2007, **111**, 11817–11823.
32 J. R. Lakowicz, Instrumentation for Fluorescence Spectroscopy, *Principles of Fluorescence Spectroscopy*, 2006, pp. 27–61.
33 S. V. Wegner, A. Okesli, P. Chen and C. He, Design of an emission ratiometric biosensor from MerR family proteins: A sensitive and selective sensor for $Hg^{2+}$, *J. Am. Chem. Soc.*, 2007, **129**, 3474–3475.
34 R. Häner, S. M. Biner, S. M. Langenegger, T. Meng and V. L. Malinovskii, A Highly Sensitive, Excimer-Controlled Molecular Beacon, *Angew. Chem., Int. Ed.*, 2010, **122**, 1249–1252.
35 P. Pramanik, S. K. Das and M. Halder, FRET-Selective and Ion-Exchange Responsive Smart Nano-GUMBOS from Functionalized Pyrene: First Observation of Excited State Aggregation (Exciaggremer) Inside Crystalline Nanoball, *J. Phys. Chem. C*, 2020, **124**, 4791–4801.
36 A. Kumar, M. Dubey, R. Pandey, R. K. Gupta, A. Kumar, A. C. Kalita and D. S. Pandey, A Schiff base and its copper(II) complex as a highly selective chemodosimeter for mercury(II) involving preferential hydrolysis of aldimine over an ester group, *Inorg. Chem.*, 2014, **53**, 4944–4955.
37 P. Holmes, K. A. F. James and L. S. Levy, Is low-level environmental mercury exposure of concern to human health?, *Sci. Total Environ.*, 2009, **408**, 171–182.
38 P. B. Tchounwou, W. K. Ayensu, N. Ninashvili and D. Sutton, Review: Environmental exposure to mercury and its toxicopathologic implications for public health, *Environ. Toxicol.*, 2003, **18**, 149–175.
39 R. A. Bernhoft, Mercury Toxicity and Treatment: A Review of the Literature, *J. Environ. Public Health*, 2012, **2012**, 460508.
40 C. T. Driscoll, R. P. Mason, H. M. Chan, D. J. Jacob and N. Pirrone, Mercury as a global pollutant: Sources, pathways, and effects, *Environ. Sci. Technol.*, 2013, **47**, 4967–4983.
41 G. Genchi, M. S. Sinicropi, A. Carocci, G. Lauria and A. Catalano, Mercury Exposure and Heart Diseases, *Int. J. Environ. Res. Public Health*, 2017, **14**, 74.
42 B. Gworek, O. Bemowska-Kałabun, M. Kijeńska and J. Wrzosek-Jakubowska, Mercury in Marine and Oceanic Waters—a Review, *Water, Air, Soil Pollut.*, 2016, **227**, 1–19.
43 S. M. Ullrich, T. W. Tanton and S. A. Abdrashitova, Mercury in the Aquatic Environment: A Review of Factors

 

Affecting Methylation, *Crit. Rev. Environ. Sci. Technol.*, 2001, **31**, 241–293.

44 A. J. Poulain, E. Garcia, M. Amyot, P. G. C. Campbell, F. Raofie and P. A. Ariya, Biological and chemical redox transformations of mercury in fresh and salt waters of the high arctic during spring and summer, *Environ. Sci. Technol.*, 2007, **41**, 1883–1888.

45 E. M. Nolan and S. J. Lippard, Tools and tactics for the optical detection of mercuric ion, *Chem. Rev.*, 2008, **108**, 3443–3480.

46 J. Wang, B. Tian, J. Lu, J. Wang, D. Luo and D. MacDonald, Remote Electrochemical Sensor for Monitoring Trace Mercury, *Electroanalysis*, 1998, **10**, 399–402.

47 G. Mor-Piperberg, R. Tel-Vered, J. Elbaz and I. Willner, Nanoengineered electrically contacted enzymes on DNA scaffolds: Functional assemblies for the selective analysis of $Hg^{2+}$ Ions, *J. Am. Chem. Soc.*, 2010, **132**, 6878–6879.

48 A. Ono, H. Togashi, A. Ono and H. Togashi, Highly Selective Oligonucleotide-Based Sensor for Mercury(II) in Aqueous Solutions, *Angew. Chem., Int. Ed.*, 2004, **116**, 4400–4402.

49 M. Dong, Y. W. Wang and Y. Peng, Highly selective ratiometric fluorescent sensing for $Hg^{2+}$ and $Au^{3+}$, respectively, in aqueous media, *Org. Lett.*, 2010, **12**, 5310–5313.

50 X. J. Zhu, S. T. Fu, W. K. Wong, J. P. Guo and W. Y. Wong, A near-infrared-fluorescent chemodosimeter for mercuric ion based on an expanded porphyrin, *Angew. Chem., Int. Ed.*, 2006, **45**, 3150–3154.

51 I. B. Kim and U. H. F. Bunz, Modulating the sensory response of a conjugated polymer by proteins: An agglutination assay for mercury ions in water, *J. Am. Chem. Soc.*, 2006, **128**, 2818–2819.

52 Y. Zhao and Z. Zhong, Tuning the sensitivity of a foldamer-based mercury sensor by its folding energy, *J. Am. Chem. Soc.*, 2006, **128**, 9988–9989.

53 J. Liu and Y. Lu, Rational Design of ''Turn-On'' Allosteric DNAzyme Catalytic Beacons for Aqueous Mercury Ions with Ultrahigh Sensitivity and Selectivity, *Angew. Chem., Int. Ed.*, 2007, **46**, 7587–7590.

54 C. K. Chiang, C. C. Huang, C. W. Liu and H. T. Chang, Oligonucleotide-based fluorescence probe for sensitive and selective detection of mercury(II) in aqueous solution, *Anal. Chem.*, 2008, **80**, 3716–3721.

55 F. Loe-Mie, G. Marchand, J. Berthier, N. Sarrut, M. Pucheault, M. Blanchard-Desce, F. Vinet, M. Vaultier, F. Loe-Mie, G. Marchand, J. Berthier, N. Sarrut, F. Vinet, M. Pucheault, M. Blanchard-Desce and M. Vaultier, Towards an Efficient Microsystem for the Real-Time Detection and Quantification of Mercury in Water Based on a Specifically Designed Fluorogenic Binary Task-Specific Ionic Liquid, *Angew. Chem., Int. Ed.*, 2010, **49**, 424–427.

56 W. Lin, X. Cao, Y. Ding, L. Yuan and L. Long, A highly selective and sensitive fluorescent probe for $Hg^{2+}$ imaging in live cells based on a rhodamine – thioamide – alkyne scaffold, *Chem. Commun.*, 2010, **46**, 3529–3531.

57 N. Dave, M. Y. Chan, P. J. J. Huang, B. D. Smith and J. Liu, Regenerable DNA-functionalized hydrogels for ultrasensitive, instrument-free mercury(II) detection and removal in water, *J. Am. Chem. Soc.*, 2010, **132**, 12668–12673.

58 J. J. Mcnerney, P. R. Buseck and R. C. Hanson, Mercury Detection by Means of Thin Gold Films, *Science*, 1972, **178**, 611–612.

59 J. Drelich, C. L. White and Z. Xu, Laboratory Tests on Mercury Emission Monitoring with Resonating Gold-coated Silicon Cantilevers, *Environ. Sci. Technol.*, 2008, **42**, 2072–2078.

60 M. Amde, Y. Yin, D. Zhang and J. Liu, Methods and recent advances in speciation analysis of mercury chemical species in environmental samples: a review, *Chem. Speciation Bioavailability*, 2016, **28**, 51–65.

61 D. K. Sarfo, A. Sivanesan, E. L. Izake and G. A. Ayoko, Rapid detection of mercury contamination in water by surface enhanced Raman spectroscopy, *RSC Adv.*, 2017, **7**, 21567–21575.

62 T. Sultana, M. Mahato, S. Ahamed, N. Tohora, J. Chourasia, S. Ghanta and S. Kumar Das, A 'Turn-on' fluorogenic probe for selective and specific detection of Hg(II) ions, *J. Photochem. Photobiol., A*, 2025, **459**, 116028.

63 M. Oguz, D. Aydin, S. Malkondu and S. Erdemir, Specific and low-level detection of $Hg^{2+}$ and $CN^{-}$ in aqueous solution by a new fluorescent probe: Its real sample applications including cell, soil, water, and food, *Sens. Actuators, B*, 2025, **433**, 137527.

64 A. Aswathy, P. K. Vineetha, V. Kandathil, J. Jose, S. G. Bhat and N. Manoj, A Simple Live Cell Imaging ''Turn–On'' Fluorescence Probe for the Selective and Sensitive Detection of Aqueous $Hg^{2+}$ Ions, *J. Fluoresc.*, 2024, **34**, 1671–1682.

65 H. Li, J. Li, Z. Pan, T. Zheng, Y. Song, J. Zhang and Z. Xiao, Highly selective and sensitive detection of $Hg^{2+}$ by a novel fluorescent probe with dual recognition sites, *Spectrochim. Acta, Part A*, 2023, **291**, 122379.

66 W. Chansuvarn, T. Tuntulani and A. Imyim, Colorimetric detection of mercury(II) based on gold nanoparticles, fluorescent gold nanoclusters and other gold-based nanomaterials, *TrAC, Trends Anal. Chem.*, 2015, **65**, 83–96.

67 J. Du, L. Jiang, Q. Shao, X. Liu, R. S. Marks, J. Ma and X. Chen, Colorimetric Detection of Mercury Ions Based on Plasmonic Nanoparticles, *Small*, 2013, **9**, 1467–1481.

68 X. Xu, Y. F. Li, J. Zhao, Y. Li, J. Lin, B. Li, Y. Gao and C. Chen, Nanomaterial-based approaches for the detection and speciation of mercury, *Analyst*, 2015, **140**, 7841–7853.

69 G. Chen, Z. Guo, G. Zeng and L. Tang, Fluorescent and colorimetric sensors for environmental mercury detection, *Analyst*, 2015, **140**, 5400–5443.

70 L. R. Pokhrel, N. Ettore, Z. L. Jacobs, A. Zarr, M. H. Weir, P. R. Scheuerman, S. R. Kanel and B. Dubey, Novel carbon nanotube (CNT)-based ultrasensitive sensors for trace mercury(II) detection in water: A review, *Sci. Total Environ.*, 2017, **574**, 1379–1388.

71 J. B. Birks, D. J. Dyson and I. Munro, 'Excimer' fluorescence II. Lifetime studies of pyrene solutions, *Proc. R. Soc. London, Ser. A*, 1963, **275**, 575–588.

72 F. Winnik, Photophysics of Preassociated Pyrenes in Aqueous Polymer Solutions and in Other Organized Media, *Chem. Rev.*, 1993, **93**, 587–614.

73 R. D. Pensack, R. J. Ashmore, A. L. Paoletta and G. D. Scholes, The Nature of Excimer Formation in Crystalline Pyrene Nanoparticles, *J. Phys. Chem. C*, 2018, **122**, 21004–21017.
74 A. Shrivastava and V. Gupta, Methods for the determination of limit of detection and limit of quantitation of the analytical methods, *Chron. Young Sci.*, 2011, **2**, 21.
75 H. A. Benesi and J. H. Hildebrand, A Spectrophotometric Investigation of the Interaction of Iodine with Aromatic Hydrocarbons, *J. Am. Chem. Soc.*, 1949, **71**, 2703–2707.
76 D. Ghosh, N. Nandi and N. Chattopadhyay, Differential Förster resonance energy transfer from the excimers of poly(*N*-vinylcarbazole) to coumarin 153, *J. Phys. Chem. B*, 2012, **116**, 4693–4701.



 